Accepted manuscript. Published in Journal of Geotechnical and Geoenvironmental Engineering (2021). Version of record: https://doi.org/10.1061/(ASCE)GT.1943-5606.0002600. This material may be downloaded for personal use only. Any other use requires prior permission of the American Society of Civil Engineers. This material may be found at https://doi.org/10.1061/(ASCE)GT.1943-5606.0002600.

Effect of water-rock interaction on the axial capacity of drilled caissons socketed in claystone bedrock

Mitul Sisodiya[1], Shubjot Singh[2], David Thomas[3], Yida Zhang[4*]

ABSTRACT

A large number of bridges and structures in Colorado are supported by drilled caissons and shafts socketed in weak clay-bearing rocks (e.g., Denver blue claystone and Pierre shale). During construction of caissons using the wet drilling technique, drilling fluid gets in direct contact with the bedrock, potentially causing their slaking and degradation and thus undermining the foundation capacity. This paper evaluates the effect of water infiltration on the axial capacity of caissons embedded in claystone. The methodology of this research combines laboratory testing and coupled finite element analysis for unsaturated porous materials. A series of experiments were conducted to determine the hydraulic characteristics and the strength-suction relations of the claystone samples obtained from three sites near Denver, Colorado. These parameters were then used in numerical studies of wet drilled caissons subjected to different wetting times (i.e., the time interval between the completion of drilling and the placement of concrete). Adopting the coupled unsaturated flow and mechanical analysis in ABAQUS, a workflow was developed for modeling the full process of drilling, fluid infiltration, caisson construction, and in-situ axial loading. The results showed that among the three sites, the immediate caisson capacity reduction was the highest (≈19%) for the most permeable and water-sensitive formation. On the other hand, the capacity reduction was found to be negligible (≈0%) if the rock was relatively intact with low permeability, regardless of its strength-suction characteristics. Parametric studies also showed that bedrocks with lower initial degree of saturation experience more rapid and significant strength reduction upon wetting. These results provide the basis to establish practical guidance to evaluate and minimize the impact of wetting time on caisson constructions.

[1] Ph.D. student, University of Colorado Boulder, Boulder, CO, USA.
[2] Graduate student, University of Colorado Boulder, Boulder, CO, USA.
[3] Engineering Geologist, Colorado Department of Transportation, CO, USA.
[4] Assistant Professor, University of Colorado Boulder, Boulder, CO, USA. Corresponding author: Yida.Zhang@Colorado.edu

INTRODUCTION

Drilled caissons have been widely used in Colorado to support bridges and other transportation structures for the majority of expansive soil sites over, approximately, the past 50 years (Claybourn 2007) . A large number of caissons are embedded in weak clay-bearing rocks such as the Denver blue claystone and the Pierre shale. These formations typically exhibit strong slaking, swelling and degradation when exposed to water. Mechanically, when equilibrated with different suctions, claystone exhibits distinct stress-strain responses (Liu and Shao 2016), with the common observation of lowered shear strength and stiffness at higher moisture level and vice versa (Guillon et al. 2012; Shao et al. 2006). Such property of claystone has caused various instability problems in geotechnical engineering practices. For instance, Irsyam et al. (1999) attributed many slope instabilities during the construction of Tulis hydroelectric power plant to the progression of rock slaking. Matsui and Shimada (1995) reported that the slaking of Ikeshima shale caused excessive roadway closures during mining operations. More recently, Miščević and Vlastelica (2014) attributed the failure of a highway cut slope in flysch formation to the seepage-induced slaking of marl underneath a sturdy sandstone layer. In the petroleum industry, extensive studies have been conducted to understand the swelling and degradation of shale immersed in various drilling fluids in the context of wellbore stability (Al-Bazali et al. 2008; Lal and Amoco 1999; Lu et al. 2014) .

So far, only a few studies have reported the impact of fluid infiltration on the bearing capacity of caissons socketed in claystone bedrocks. During the construction of drilled shaft foundations for the New Carquinez Bridge, Chang et al. (2004) had encountered soft claystone characterized by high potential for slaking, swelling and softening when in contact with the polymer slurry. As a way of mitigation, 6% of salt was added to the slurry, after which the construction was completed successfully. Claybourn (2007) reported a case in northwest Denver where some drilled piers bearing on claystone experienced plunging failure. Post-failure inspections found that the claystone was highly fissured and had high slaking and dispersion potentials. In addition, the site was characterized by high groundwater levels. Excavation of the failed piers revealed a large zone of softened claystone, characterized by high moisture content and extremely low shear strength at the pier-rock interface. It was believed that the infiltration of ground water into the fissures has completely deteriorated the rock mass and caused the failure of the piers. These cases suggest that water-rock interaction in claystone can have serious impacts on the construction and the functionality of deep foundations.

To safeguard against these adverse effects, the Colorado Department of Transportation (CDOT) has stipulated a maximum four hours limit on the duration between the completion of drilling and the placement of concrete (hereinafter referred to as "wetting time"). In cases that the contractors exceeded such time limitation, the remedial action is to extend the drilling depth for one-third of the originally planned embedment. However, no systematic laboratory or field-scale studies were used to arrive at the four-hour time limit beyond their engineering judgement. The true time limit to avoid excessive degradation can be highly dependent on site-specific conditions, such as the water-sensitivity of the rock, the degree of fissuring and the in-situ degree of saturation. The objective of this study is to fill this knowledge gap and provide some references to determine the maximum allowable wetting time according to site conditions. Considering that water has a stronger interacting with clay rocks than polymer- or slurry-based drilling fluids (Hemphill et al. 2008; Karakul 2018), this pilot study is focused on the water-induced degradation of claystone. The study is conducted in two phases: experimental and numerical. The experimental phase involved determination of shear strength and hydraulic properties of Denver blue claystone samples. In the numerical phase, the reduction of axial capacity of drilled caissons due to water infiltration was evaluated using coupled finite element analysis.

EXPERIMENTAL PROGRAM

Claystone Samples

The in-situ claystone samples investigated in this study were obtained via core drilling from three Denver sites: I-70 & Colfax (39°44'26.6"N 104°43'41.3"W), I-70 & Wadsworth (39°47'09.6"N 05°04'52.9"W) and C-470 & Wads (39°33'14.3"N 105°05'05.5"W), hereinafter referred to as Site-1,2 and 3, respectively. The specimens were cut to size from the drilled cores (63.5 mm diameter) by carbide saw without using water. The required specimen heights varied depending on the experiment and are detailed in the experiment procedures below. Table 1 reports the dry unit weight, the natural water content, the specific gravity of solids (ASTM:D854-14), and the index properties (ASTM:D4318-17e1) of the claystone samples from all three sites. The testing campaign included: 1) preparing uniform unsaturated samples at different suctions for direct shear tests and for soil water retention curve (SWRC) data points, 2) flex-wall permeameter tests to determine the saturated hydraulic conductivity and 3) direct shear tests to determine the peak and residual shear strength of variably saturated samples.

Testing Procedure

There is a variety of SWRC measurement techniques available in the literature depending on the suction range and the type of material. This includes the traditional techniques like hanging column, pressure extractor, and chilled mirror hygrometer (ASTM:D6836-16), as well as more advanced setups that can measure the SWRC curve and the hydraulic conductivity function simultaneously (Lu et al. 2006; Lu and Kaya 2013; Wayllace and Lu 2012) and fully automated systems (Likos and Lu 2003). Considering the requirement of preparing direct shear test samples at specific suction levels with uniform partial saturation and time constraints involved in this project, the SWRC was determined using the vapor equilibrium technique.

Vapor equilibrium was achieved by placing the samples in sealed desiccators (Fig. 1a) together with saturated salt solutions (Blatz et al. 2008; Delage et al. 1998; Leong and Rahardjo 2002; Pineda et al. 2014). The saturated salt solution serves as a regulator of the relative humidity in the desiccator which also provides a constant and uniform suction on the sample. Four salts were selected to represent a wide range of suction and to avoid the use of highly toxic substances. Table 2 lists the salt solutions along with their corresponding total suction computed by the Kelvin's law. Specimens of about 5 mm thickness (mass between 30-40 gm) were cut from the cores and then further broken into small chunks (10-15 mm length and width). The specimens were then placed into the four desiccators and the lid was carefully sealed with vacuum grease. Samples were taken out every five to six days to measure the mass change due to vapor exchange. Fig. 1b plots the variation of specimen mass with respect to time for the desiccator (RH=11.31%) as an example. Equilibrium was assumed when the specimen mass became constant to the precision of the balance (0.01 grams) and became oscillating around the mean value (in the range of 0.03 grams). Once the specimens were equilibrated, the degree of saturation was measured using a non-polar fluid displacement technique (Ferrari et al. 2014; Peron et al. 2007) which can account for the volume change of the specimen during wetting/drying. The non-polar fluid used in this study was a commercially available kerosene "KLEAN HEAT" with a density of 789.7 kg/m^3 at a standard temperature of 15℃. The kerosene density was corrected to the experiment temperature (ASTM:D1250-04) for calculations. The saturated hydraulic conductivity was determined using the flex-wall permeameter procedure (ASTM:D5084-16a method-C) which consists of three phases: soaking, back-pressure saturation, and hydraulic conductivity measurement. Specimens of about 100 mm height and free of large cracks visible on the surface were used.

112 To determine the peak and residual shear strength parameters at varying saturations, a total of 64 direct
113 shear tests were performed on the claystone samples from all sites. Samples were prepared at the four
114 suction levels again via the vapor equilibrium technique using the salt solutions described in Table 2. The
115 specimens had a cylindrical geometry with a height of about 45 mm and diameter between 60-64mm after
116 reaching equilibrium. The equilibrium time was found to be about 30 days after which the rate of moisture
117 change became negligible for all specimens. When preparing the specimens, encapsulating materials for
118 routine rock mechanics testing could not be used here because their long hardening period would cost
119 significant moisture variation of the claystone samples. To accommodate the need of fast sample
120 assemblage and testing, a split cylindrical direct shear box was designed and fabricated to secure the
121 sample tightly and rapidly. The direct shear box consists of a loading cap, a top ring, and a bottom ring
122 connected to a bottom plate as shown in Fig. 2a. The vertical gap between the two sections is adjustable
123 to accommodate samples with slight size variations. In preparing each sample, the specimen was taken
124 out of the desiccator and placed at the center of the bottom plate in contact with half of the bottom ring.
125 The other half of the bottom ring was then fastened so that the sample was well secured in the shear box.
126 The top ring was then similarly installed, leaving a 1mm gap with the bottom ring. Additional lubrication
127 was applied at the bottom of the top ring to avoid friction during shearing. After the assembly of the shear
128 box, the unit was placed on a conventional direct shear device. The normal load was applied through a
129 dead load system and the sample was sheared at a rate of 1 mm/min using an electric motor and gearbox
130 system. The selected shear velocity is slow enough to have negligible rate effect and also not too slow to
131 avoid loss of moisture during testing. The load-displacement curve was observed in real-time and the peak
132 and residual states were identified graphically. The load was measured by a load cell and the vertical and
133 horizontal displacements were measured by LVDTs in accordance with ASTM D5607-16. Test data was
134 electronically recorded using National Instrument hardware and LabVIEW software at a frequency of 100
135 Hz. Fig. 2b shows the direct shear box, assembled, and connected to the shearing machine.

136 ***Experimental Results***

137 The obtained SWRC data are plotted in Fig. 3 and fitted by the Van Genuchten equation (Van Genuchten
138 1980) for the numerical analysis later:

139 $$S_e = \frac{S - S_r}{1 - S_r} = \left(\frac{1}{1 + (\alpha\psi)^n} \right)^{1-1/n} \quad (1)$$

Where S_e is the effective degree of saturation; S the degree of saturation; S_r the residual degree of saturation; ψ the total suction; parameter α approximately equal to the inverse of the suction air entry value (AEV) and n governs the steepness of the SWRC. The calibrated SWRC parameters are collected in Table 3. The saturated hydraulic conductivity values, obtained using the flex-wall permeameter, are presented in Table 4.

A typical set of load-displacement curves from the direct shear test is plotted in Fig. 4. These curves were obtained from Site-1 specimens subjected to the same normal load 351.5 N (corresponding to σ_v=115 to 120 kPa) but prepared at different suctions. The peak and the residual states are marked on the figure for one of the curves. As seen from the figure, the specimens prepared at higher suction (lower degree of saturation) had higher strength with brittle response. The load-displacement curve became more ductile and the strength reduced as the suction decreased. Photos of high-suction (s=294.29 MPa) and low-suction (s=3.29 MPa) specimens after shearing are shown in Fig. 5. It can be seen that the failure plane of the specimen prepared at low suction was quite homogenous with dispersed grains (Fig. 5a), while that of the specimen prepared at high suction was more irregular and sharper (Fig. 5b). The observations from Fig. 4 and Fig. 5 can be explained by considering the interaction between rock matrix and microcracks. At low suction, the intrinsic shear strength of the bulk material is relatively low. The "soft" matrix can help smear the stress concentration caused by local heterogeneities or microcracks during loading, thus resulting in an overall ductile response and a uniform slip surface. In contrast, at high suction, the claystone matrix becomes more brittle and has a higher intrinsic shear strength. Microcracks in brittle matrixes can give high stress concentrations when loaded, causing the overall strength of the sample dominated by the propagation and coalescence of microcracks. The slip plane formed after crack coalescence is therefore more irregular, producing a sudden drop in the overall load-displacement curve.

The peak and residual failure data and the best-fit envelopes of the claystone samples from Site-1, 2 and 3 are shown in Fig. 6, Fig. 7 and Fig. 8, respectively. The Mohr-Coulomb envelope for peak strength is given by:

$$\tau_p = c_p + \sigma_n \tan\phi_p \tag{2}$$

where σ_n is the total normal stress; τ_p the peak shear stress; ϕ_p and c_p the peak friction angle and peak cohesion, respectively. The Mohr-Coulomb envelope for residual strength is similar to Eq. (2) except that

the subscript '*p*' is replaced by "*r*'. As expected, it was observed that both the peak and residual strength increased with increasing suction or reducing degree of saturation. Some large scatters are observed from specimens that have higher suction levels (making the sample dryer and more brittle) and/or relatively high shear strengths (Site-1 and Site-3). This is because, as discussed previously, microcracks dominates the apparent shear strength of specimens made of more brittle and tougher solid matrixes. The propagation and coalescence of microcracks is highly sensitive to the initial orientation, density, and size of microcracks (Hamdi et al. 2015; Li et al. 2018; Sisodiya and Zhang 2020; Wong et al. 1996) and therefore can induce large uncertainties in the strength measurements. Similar data scatter has been also observed in the shear strength vs. moisture curves of argillaceous rocks in other studies (Zhang et al. 2014; Zhang et al. 2013). Another observation was that the residual cohesion is zero for all the sites irrespective of the suction level. This is because, at residual stage, all the bonds along the failure plane are broken, and the remaining shear resistance is solely contributed by the frictional force which is proportional to the normal stress at the slip surface. This is consistent with observations from other studies on stiff overconsolidated clays (Lupinl et al. 2009; Skempton 1985; Stark and Eid 1994). The peak and residual strength parameters calibrated from Fig. 6~Fig. 8 are summarized in Table 5.

The variation of ϕ_p, ϕ_r and c_p with respect to suction is plotted in Fig. 9 and Fig. 10, respectively. The tangent of the peak and the residual friction angles were fitted using a log-linear relationship with respect to suction also shown in Fig. 9:

$$\tan\phi_p = a_p \log\left(\frac{\psi}{\psi_{ref}}\right) \tag{3}$$

$$\tan\phi_r = a_r \log\left(\frac{\psi}{\psi_{ref}}\right) \tag{4}$$

where $\psi_{ref} = 1$ kPa is a reference suction; a_p and a_r are fitting parameters.

The cohesion-suction data for the peak envelope is plotted in Fig. 10. Observing the nonlinear trend of these curves in the semilogarithmic plot, additional direct shear tests were conducted on fully saturated samples to determine their intersections with the y-axis (open symbols in Fig. 10). Based on this data, the peak cohesion was fitted by the following equation:

193 $$c_p = c_{p1} + c_{p2}\left(\log\frac{\psi}{\psi_{ref}}\right)^2 \quad (5)$$

194 where c_{p1} and c_{p2} are two fitting parameters. It is worth noting that Eqs. (3)~(5) are only applicable for
195 suctions higher than the reference value ψ_{ref}. Below this value the strength parameters are taken to be
196 constant. The parameters in Eqs. (4) and (5) for all three sites are summarized in Table 6.

197 **FINITE ELEMENT ANALYSIS**

198 This section presents a series of numerical simulations investigating the effect of drilling fluid infiltration
199 on the axial capacity of caissons socketed in claystone bedrocks. Many field tests has been conducted on
200 this type of foundations (Abu-Hejleh et al. 2003; Abu-Hejleh and Attwooll 2005). However, none of them
201 have focused on the variation of axial capacity as a function of wetting time. The following numerical
202 study is intended as a pilot study to evaluate the potential effect of wetting time, which may motivate
203 future full-scale field investigations on this subject.

204 Finite Element Analyses (FEA) were performed using the general-purpose Finite Element software
205 ABAQUS to study the reduction of axial load capacity of drilled caissons due to excessive wetting. A
206 coupled pore fluid diffusion and effective stress analysis was used to model both the partially and the fully
207 saturated domains. Fluid flow is governed by the generalized Darcy's law and the claystone is described
208 by a Mohr-Coulomb elasto-perfect-plastic model in effective stress space. The program iteratively solves
209 the diffusion equation (or the mass balance of water) and the equilibrium condition using fully implicit
210 Newton-Raphson algorithm in the ABAQUS Standard solver. A user-defined field subroutine (USDFLD)
211 was implemented to update the strength parameters of claystone with respect to the field variables
212 (saturation and pore pressure in this study) during each iteration.

213 ***Model Geometry and Mesh***

214 The model geometry shown in Fig. 11 depicts a typical caisson design in Denver area (Abu-Hejleh and
215 Attwooll 2005). Soil above the claystone formation (approximately 8.8 m deep) was not directly simulated
216 but included as an overburden pressure of 145.8 kPa assuming a moist unit weight of 16.5 kN/m^3.
217 Similarly, 5.8 m of the caisson below the ground surface was replaced by an equivalent pressure of 136.5
218 kPa applied on top of the simulated caisson segment. At initial state, the pore pressure is assumed to be

hydrostatic with the water table set at 21.0 m below the ground level (7.6 m below the caisson tip). The water table depth is based on the data from a monitoring station situated in Douglas County (close to Site-3). The station is maintained by United States Geological survey Colorado Water Science Centre (USGS 2019) and has been recording the groundwater level for Denver Basin aquifer in Douglas county since 2011. In this study, the data from 2011 to 2019 was considered and the average value was taken. A total of 916 CAX8P (eight-node axisymmetric quadrilateral, biquadratic displacement, bilinear pore pressure) elements were used in the model for coupled hydromechanical analysis (i.e., the "soil" step in ABAQUS). The mesh sizes for the caisson and the claystone were determined according to Sheng et al. (2005) and Bäker (2018) which suggests that the optimal size of the soil element should be about 1~1.5 times of the size of the pile element to obtain convergent solution.

Parameters and Steps

Three sets of claystone parameters corresponding respectively to Site-1, 2 and 3 bedrock were used in the simulations. For each site, the fitted SWRC curve was directly used as the input. The hydraulic conductivity function (HCF) was assumed to obey the following equation (Irmay 1954):

$$k = K_{sat} S_e^3 \tag{6}$$

where K_{sat} is experimentally determined in Table 4. This HCF was also used in other finite element studies (Alonso et al. 2003; Fredlund 2006) to model the fluid flow through unsaturated soils. On the mechanical aspect, the Claystone was modelled as a linear elasto-perfect-plastic material obeying Mohr-Coulomb failure in Bishop's effective stress space. The suction-dependent effective strength parameters such as effective cohesion and friction angle for claystone were derived from the total strength parameters measured in subsection "Experimental Results" and then implemented through the USDFLD which is discussed in the next section. Due to the lack of stress-strain measurements, the elastic properties of the Denver formation were taken from Abu-Hejleh and Attwooll (2005) which were determined by in-situ testing. The dilation angle was taken as zero since the amount of dilatancy observed in the direct shear test was negligible. The concrete caisson was modelled as a linear elastic material with the elastic properties reported in Seo et al. (2008). The parameters used in the simulation (except for strength parameters) for the claystone and the concrete caisson are listed in Table 7**.** The interface between claystone and caisson was modeled as hard contact using penalty method with a friction coefficient of 0.6. This value was chosen based on studies on interface-friction between concrete and smooth rock surface

(Nasir and Fall 2008; Tian et al. 2015) to represent a conservative estimation of the friction coefficient along the caisson-claystone interface.

To best reproduce the in-situ hydraulic and stress paths, the full process of caisson construction including drilling, wetting and pile installation were simulated prior to in-situ axial load testing. A total of five steps were simulated in the finite element model: geostatic balance (Step I), drilling fluid infiltration (Step II), caisson installation (Step III), friction activation at the interface (Step IV), and axial loading test (Step V). Fig. 12 shows the schematic of each step.

In the first step, gravity was applied to the claystone with the caisson element deactivated. The side of the borehole was constrained by a slider boundary to prevent collapse. The heaving of the bottom was prevented by a pressure equal to the total overburden at the depth of the pile tip. Since effective stress analysis was used, the initial stress field must be assigned with the effective values based on Bishop's definition (Bishop 1954):

$$\sigma'_{ij} = \sigma_{ij} + \chi\psi\delta_{ij} \qquad (7)$$

where σ'_{ij} is the effective stress; σ_{ij} the total stress; δ_{ij} the Kronecker delta; χ the Bishop's stress coefficient which is taken as the degree of saturation S in ABAQUS. By assuming a hydrostatic suction distribution, the initial effective stresses were calculated according to Eq. (7) and assigned to the model. The values of the initial degree of saturation were then computed and assigned to the domain using the initial hydrostatic pore pressure distribution together with the SWRC of each Site. Geostatic balance was verified by observing zero deformations at the end of this step. In the second step, a hydrostatic pore pressure boundary at the bottom and the lateral surface of the borehole was imposed (see Fig. 11) to simulate the infiltration of drilling fluid in the claystone prior to concrete placement. Four wetting durations (2 hours, 4 hours, 8 hours, and 16 hours) were studied to represent the typical construction scenarios. The saturation contours after 16 hours of wetting for the three sites are shown in Fig 13. After 16 hours of wetting, Site-2 and 3 had similar size of the infiltration zone, both larger than that of the Site-1. In the third step, the placement of concrete in the borehole was simulated. The lateral constraint on the borehole was removed, then the caisson element was activated instantly with its weight linearly increased to full over 0.5 hours. At the same time, the equivalent overburden pressure applied at the bottom of the borehole was linearly removed to prevent heaving of the bottom as well as to mimic the gradual

displacement of the drilling fluid by the concrete. In the fourth step, friction was activated by assigning a frictional coefficient of 0.6 at the concrete-rock interface to simulate the hardening of concrete paste into solid form. Then a total of two hours was provided to let the caisson settle down and equilibrate with the surrounding stress field before the axial load testing. In the final step, axial load was applied via a uniformly distributed pressure on the top of the pile with a loading rate of 27.05 MN/hr. The displacement data was collected at the top of the pile for constructing the load-displacement curves.

User Defined Field (USDFLD) Implementation

The strength parameters at each material point were updated with respect to the local degree of saturation via a USDLFD. As mentioned in the previous section, ABAQUS relies on effective stress to update the strain and displacement fields for porous materials and thus require effective strength parameters in the Mohr-Coulomb model. The strength-suction relations (Eqs. (3), (4) and (5)) determined by the experiments, however, were established based on total stress. To obtain strength parameters in terms of effective stress, the total stress in Eq. (2) was replaced by the effective stress using Eq. (7) (See Lu and Likos 2006):

$$\tau_p = c_p + \left(\sigma_n' - S\psi\right)\tan\phi_p = \left(c_p - S\psi\tan\phi_p\right) + \sigma_n'\tan\phi_p \tag{8}$$

Comparing Eq. (8) with the effective Mohr-Coulomb criterion, the effective cohesion c' and the effective friction angle ϕ' are obtained as:

$$c' = c_p - S\psi\tan\phi_p \tag{9}$$

$$\phi' = \phi_p \tag{10}$$

Having established the variation of ϕ_p and c_p with suction and the SWRC relation in subsection "Experimental Results", Eqs. (8)-(10) completes the strength-effective stress-saturation relationship (Lu et al. 2010). In the USDFLD, the degree of saturation and pore pressure were extracted and stored as state variable 1 and 2, respectively. Then the effective friction angle and cohesion were calculated based on Eqs. (3), (5), (9) and (10) in the USDFLD and were stored as field variable 1 and 2, respectively. A one-to-one relation was enforced in the ABAQUS between the field variables and the strength parameters to update the finite element computation. Fig. 14 depicts the workflow of USDFLD.

RESULTS

Simulation Results

A total of 15 simulations were conducted with different wetting times including no wetting, 2 hours, 4 hours, 8 hours, and 16 hours for all three sites. Fig. 15 shows the predicted load-displacement curves with the ultimate axial load capacities determined by the Davisson's method (Davisson 1972). Fig. 15a suggests that the degradation of the claystone for Site-1 was negligible as there was no reduction in the ultimate capacity with increasing wetting times. This was because, although the Site-1 claystone had some degree of water sensitivity (Fig. 6), its low hydraulic conductivity did not allow much fluid infiltration into the adjacent formation in the given durations (Fig. 13a), thus producing virtually no effect on the load-displacement performance. This was not the case for Site-2 where the fully saturated zone rapidly expanded (Fig. 13b), significantly weakening the rock mass behind the wetting front. It is observed from Fig. 15b that the axial resistance mobilized by the same displacement was less for longer wetting time for Site-2, consequently resulting in reduced ultimate axial load capacity. Similar results were obtained for Site-3 as seen in Fig. 15c. The shape of the load-displacement curve of Site-3 was slightly different than Site-2 in the sense that the caisson still had some significant strength gain after passing the failure point defined by Davisson's criterion. This is because of the overall higher friction angle of Site-3 claystone than the Site-2 claystone at all suction levels, giving higher strength boost as the mean stress field increased due to caisson displacement. The reduction of ultimate capacity with respect to wetting time is plotted in Fig. 16 and summarized in Table 8 where the capacity obtained without wetting is used as the reference value to calculate the percentage reduction. It is observed that Site-3 caisson had higher bearing capacity than Site-2 at all wetting times, and the percentage loss of bearing capacity for Site-3 caisson was less than that of Site-2 caisson at shorter wetting times. However, the bearing capacity of Site-3 caisson reduced more rapidly with increasing wetting time, making it more susceptible to fluid weakening at longer wetting times with 33.16% reduction after 16 hours of wetting as compared to the 31.08% reduction of Site-2 caisson. After the four-hour wetting time limited by CDOT, the relative reduction for Site-1, 2 and 3 are 0%, 18.65% and 14.77% respectively. This large variation confirms that the wetting degradation of drilled caisson is highly site dependent. It is worth to note that, although the claystone at all sites showed considerable variation in strength with changing saturation, Site-2 and 3 exhibited higher bearing capacity reduction than Site-1 simply because of the larger saturated zone formation after wetting. It is also observed that Site-3 showed more rapid strength reduction than Site-2 (Fig. 16) despite they had almost the same range of fully saturated zone (Fig. 13). This may be attributed to the relatively drier in-situ

condition of Site-3 in comparison to Site-2 (Fig. 13). These observations suggest that the hydraulic conductivity and the initial degree of saturation of the rock mass dominates the extent of axial capacity reduction for the sites studied in this paper. A further implication is that the main factors to be considered in improving the CDOT's Drill Caisson Specification 503 should not only include the strength-saturation relation but also consider the permeability of the bedrock and the initial moisture distribution at the site. Parametric studies were conducted in the next section to further verify this argument.

Parametric Analysis

Two sets of parametric studies were performed with (1) varying saturated hydraulic conductivity and (2) varying depth of in-situ water table. The latter was to understand the impact of initial moisture distribution of the bedrock on the capacity degradation of caissons, since the location of the ground water table and the saturation profile is likely to vary seasonally for a given site location. The baseline strength and hydraulic parameters are shown in Table 9. Fig. 17 shows the results of 43 simulations where each data point is a result of one complete simulation of the pile construction and axial loading process as described in the previous section. It can be seen from Fig. 17a that increasing K_{sat} accelerates the initial reduction of caisson capacity. Such effect becomes less important as the degree of saturation contour approaches the steady-state distribution. The effect of varying water table depth on the ultimate axial load capacity is shown in Fig. 17a. The different caisson capacity at zero wetting time is due to the different in-situ moisture distribution prior to the wetting. For higher water table, the overall suction in the rock mass is lower, resulting in lower shear strength and hence lower axial capacity. For a given wetting time, the axial capacity is lower when the in-situ water table is higher. This difference is more pronounced for short wetting duration and become less evident at longer wetting times. To highlight the relative loss, the normalized ultimate capacity is plotted in Fig. 18, where the capacity at zero wetting time is taken as the reference value. It is also observed that the relative degradation for lower values of wetting time (up to 10 hours) is almost independent of the depth of water table, and the effect of water table becomes more pronounced as the wetting time increases. One can conclude that the more saturated the in-situ rock is, the less impact the wetting will have on the caisson capacity. This conclusion justifies the higher reduction in strength for Site-3 as compared to Site-2, despite of the fact that Site-2 and 3 have similar width of infiltrated zone.

CONCLUSION AND DISCUSSION

This study presented the results of an experimental campaign on the mechanical and hydraulic properties of claystone samples obtained from three locations in Denver, CO. The calibrated parameters were input to a coupled finite element model of a single drilled caisson subjected to wetting and loading. The main conclusions are:

1. For the sites studied in this paper, the hydraulic conductivity and the initial degree of saturation of the rock mass dominates the extent of wetting-induced axial capacity reduction of caissons.
2. Increased hydraulic conductivity can accelerate caisson capacity reduction at short wetting durations but becomes less important when the system approaches to steady state.
3. Conversely, different initial suction profiles in the bedrock do not affect much the capacity reduction characteristics for short wetting times but become more significant at longer durations.

Based on these findings, it is recommended that for dry, highly weathered or fissured claystone with a relatively high hydraulic conductivity, the time interval between the completion of drilling and the placement of concrete should be tightly constrained to avoid excessive degradation of the rock matrix. It is worth to note that the predicted relative reduction of the axial capacity in this study is rather exaggerated (i.e., on the conservative side) because of the following reasons: 1) the direct shear tests were conducted parallel to the bedding plane which is the weakest direction in resisting shearing and is more sensitive to wetting; 2) the current strength tests were conducted with pure water as the infiltration fluid which gives the most slaking effect of the claystone compared to other types of drilling fluid such as polymer slurry or salt water (Hemphill et al. 2008; Karakul 2018); 3) the concrete hardening time was very short (two hours) and no time was given between the completion of the caisson and the axial load test, thus the moisture near the caisson had little time to re-equilibrate with the adjacent rocks, producing a very conservative scenario. Considering the above factors, we believe that the current 4-hour limitation required by CDOT is reasonable and perhaps on the conservative side. Future improvements of CDOT's specification on wetting time may include more site-specific variables including the in-situ moisture content and the permeability of the bedrock.

Despite the integrated experimental and numerical effort in this work, a lot more to learn about the effect of drilling fluid infiltration on the weakening of claystone bedrocks and its impacts on caissons. Centrifuge tests, intermediate-scale physical models, and full-scale field tests could help systematically quantify the extent of capacity reduction after compared to cases without fluid infiltrations. The laboratory program

391 can be further enriched by conducting suction-controlled triaxial tests to better understand the effect of
392 wetting on the stress-strain behavior of claystone samples as well as the anisotropic reduction of their
393 shear strength and stiffness. Numerical wise, introducing a “recovery” phase between the end of caisson
394 construction and the axial load test will permit a more realistic representation of the field conditions.
395 Nevertheless, the present study offers a basic framework in studying how the caisson performance is
396 affected by the hydraulic states of the clay-bearing bedrock. The workflow can be extended in follow-up
397 studies to investigate the effect of other variables such as the types of drilling fluid or caisson geometry
398 on capacity reduction.

399 **DATA AVAILABILITY STATEMENT**

400 Some or all data, models, or code that support the findings of this study are available from the
401 corresponding author upon reasonable request.

402 **ACKNOWLEDGEMENT**

403 Yida Zhang wishes to thank the funding provided by the Colorado Department of Transportation
404 through project 218.03 and the start-up fund provided by the Department of Civil, Environmental and
405 Architectural Engineering at the University of Colorado Boulder.

406 **REFERENCES**

407

408 Abu-Hejleh, N., O'Neill, M., Hanneman, D., and Attwooll, W. 2003. "Improvement of the geotechnical
409 axial design methodology for Colorado's drilled shafts socketed in weak rocks." *Transportation*
410 *Research Record: Journal of the Transportation Research Board*(1936), 100-107
411 Abu-Hejleh, N., and Attwooll, W. J. 2005. "Colorado's Axial Load Tests on Drilled Shafts Socketed in
412 Weak Rocks: Synthesis and Future Needs."
413 Al-Bazali, T., Zhang, J., Chenevert, M. E., and Sharma, M. M. 2008. "Factors controlling the
414 compressive strength and acoustic properties of shales when interacting with water-based fluids."
415 *International Journal of Rock Mechanics and Mining Sciences*, 45(5), 729-
416 738.https://doi.org/10.1016/j.ijrmms.2007.08.012
417 Alonso, E. E., Gens, A., and Delahaye, C. H. 2003. "Influence of rainfall on the deformation and
418 stability of a slope in overconsolidated clays: a case study." *Hydrogeology Journal*, 11(1), 174-
419 192.10.1007/s10040-002-0245-1
420 ASTM International. 2014. "*D854-14* Standard Test Methods for Specific Gravity of Soil Solids by
421 Water Pycnometer." https://doi.org/10.1520/D0854-14
422 ASTM International. 2004. "*D1250-04* Standard Guide for Use of the Petroleum Measurement Tables."
423 https://doi.org/10.1520/D1250-04
424 ASTM International. 2017. "*D4318-17e1* Standard Test Methods for Liquid Limit, Plastic Limit, and
425 Plasticity Index of Soils." https://doi.org/10.1520/D4318-17E01

ASTM International. 2016. "*D5084-16a* Standard Test Methods for Measurement of Hydraulic Conductivity of Saturated Porous Materials Using a Flexible Wall Permeameter." https://doi.org/10.1520/D5084-16A

ASTM International. 2016. "*D5607-16* Standard Test Method for Performing Laboratory Direct Shear Strength Tests of Rock Specimens Under Constant Normal Force." https://doi.org/10.1520/D5607-16

ASTM International. 2016. "*D6836-16* Standard Test Methods for Determination of the Soil Water Characteristic Curve for Desorption Using Hanging Column, Pressure Extractor, Chilled Mirror Hygrometer, or Centrifuge." https://doi.org/10.1520/D6836-16

Bäker, M. 2018. "How to get meaningful and correct results from your finite element model." *arXiv preprint arXiv:1811.05753*

Bishop, A. W. 1954. "The Use of Pore-Pressure Coefficients in Practice." *Géotechnique*, 4(4), 148-152.10.1680/geot.1954.4.4.148

Blatz, J. A., Cui, Y.-J., and Oldecop, L. 2008. "Vapour equilibrium and osmotic technique for suction control." *Laboratory and Field Testing of Unsaturated Soils*, Springer, 49-61.

Chang, C.-Y., Legaspi, J., Dante E, Ma, Y., Chin, C.-C., and Orsolini, G. I. 2004. "Design, Testing and Construction of Rock Socket for Tower Foundations of the New Carquinez Bridge." *Geotechnical Engineering for Transportation Projects*, 1229-1238.

Claybourn, A. F. 2007. "Failure of Drilled Piers in Denver Due to Formation of Softened Claystone." *Contemporary Issues In Deep Foundations*, 1-11.

Davisson, M. 1972. "High capacity piles." *Proc. Innovations in Found. Const.*, 52

Delage, P., Howat, M., and Cui, Y. 1998. "The relationship between suction and swelling properties in a heavily compacted unsaturated clay." *Engineering geology*, 50(1-2), 31-48.https://doi.org/10.1016/S0013-7952(97)00083-5

Ferrari, A., Favero, V., Marschall, P., and Laloui, L. 2014. "Experimental analysis of the water retention behaviour of shales." *International Journal of Rock Mechanics and Mining Sciences*, 72, 61-70.https://doi.org/10.1016/j.ijrmms.2014.08.011

Fredlund, D. G. 2006. "Unsaturated Soil Mechanics in Engineering Practice." *Journal of Geotechnical and Geoenvironmental Engineering*, 132(3), 286-321.doi:10.1061/(ASCE)1090-0241(2006)132:3(286)

Guillon, T., Giot, R., Giraud, A., and Armand, G. 2012. "Response of Callovo-Oxfordian claystone during drying tests: unsaturated hydromechanical behavior." *Acta Geotechnica*, 7(4), 313-332.https://doi.org/10.1007/s11440-012-0172-9

Hamdi, P., Stead, D., and Elmo, D. 2015. "Characterizing the influence of stress-induced microcracks on the laboratory strength and fracture development in brittle rocks using a finite-discrete element method-micro discrete fracture network FDEM-μDFN approach." *Journal of Rock Mechanics and Geotechnical Engineering*, 7(6), 609-625.https://doi.org/10.1016/j.jrmge.2015.07.005

Hemphill, T., Abousleiman, Y. N., Tran, M. H., Hoang, S., and Nguyen, V. 2008. "Direct strength measurements of shale interaction with drilling fluids." *Proc., Abu Dhabi International Petroleum Exhibition and Conference*, Society of Petroleum Engineers.

Irmay, S. 1954. "On the hydraulic conductivity of unsaturated soils." *Eos, Transactions American Geophysical Union*, 35(3), 463-467.https://doi.org/10.1029/TR035i003p00463

Irsyam, M., Tami, D., Sadisun, I., Karyasuparta, S., and Tatang, A. 1999. "Solving landslide problem in shale cut slope in the construction of the valve chamber of the Tulis Hydroelectric Power." *Proc., Proceedings*, 217-224.

Karakul, H. 2018. "Effects of drilling fluids on the strength properties of clay-bearing rocks." *Arabian Journal of Geosciences*, 11(16), 450.https://doi.org/10.1007/s12517-018-3816-8

Lal, M., and Amoco, B. 1999. "Drilling fluid interaction and shale strength." *Proc., SPE Latin American and Caribbean Petroleum Engineering Conference. Venezuela: Society of Petroleum Engineers, SPE-1199-0030-JPT*.
Leong, E., and Rahardjo, H. 2002. "Soil-water characteristic curves of compacted residual soils." *Proc., Unsaturated soils. Proceedings of the 3rd international conference on unsaturated soils (UNSAT 2002), Recife, Brazil*, 271-276.
Li, X., Qi, C., and Shao, Z. 2018. "A microcrack growth-based constitutive model for evaluating transient shear properties during brittle creep of rocks." *Engineering Fracture Mechanics*, 194, 9-23.https://doi.org/10.1016/j.engfracmech.2018.02.034
Likos, W. J., and Lu, N. 2003. "Automated humidity system for measuring total suction characteristics of clay." *Geotechnical Testing Journal*, 26(2), 179-190.https://doi.org/10.1520/GTJ11321J
Liu, Z., and Shao, J. 2016. "Moisture effects on damage and failure of Bure claystone under compression." *Géotechnique Letters*, 6(3), 182-186.https://doi.org/10.1680/jgele.16.00054
Lu, N., Wayllace, A., Carrera, J., and Likos, W. J. 2006. "Constant flow method for concurrently measuring soil-water characteristic curve and hydraulic conductivity function." *Geotechnical Testing Journal*, 29(3), 230-241. https://doi.org/10.1520/GTJ12637
Lu, N., and Kaya, M. 2013. "A Drying Cake Method for Measuring Suction-Stress Characteristic Curve, Soil-Water-Retention Curve, and Hydraulic Conductivity Function." *Geotechnical Testing Journal*, 36(1), 1-19.https://doi.org/10.1520/GTJ20120097
Lu, N., Kaya, M., and Godt, J. W. 2014. "Interrelations among the soil-water retention, hydraulic conductivity, and suction-stress characteristic curves." *Journal of Geotechnical and Geoenvironmental Engineering*, 140(5), 04014007.https://doi.org/10.1061/(ASCE)GT.1943-5606.0001085
Lu, N., and Likos, W. J. 2006. "Suction stress characteristic curve for unsaturated soil." *Journal of Geotechnical and Geoenvironmental Engineering*, 132(2), 131-142.10.1061/(Asce)1090-0241(2006)132:2(131)
Lu, N., Godt, J. W., and Wu, D. T. 2010. "A closed-form equation for effective stress in unsaturated soil." *Water Resour Res*, 46.Artn W05515

10.1029/2009wr008646
Lupinl, J., Skinner, A., and Vaughan, P. 2009. "The drained residual strength of cohesive soils." *Selected papers on geotechnical engineering by PR Vaughan*, Thomas Telford Publishing, 88-120.
Matsui, K., and Shimada, H. 1995. "Some factors influencing stability of longwall gateroad." *Proc., International Journal of Rock Mechanics and Mining Sciences and Geomechanics Abstracts*, 409A-410A.
Miščević, P., and Vlastelica, G. 2014. "Impact of weathering on slope stability in soft rock mass." *Journal of Rock Mechanics and Geotechnical Engineering*, 6(3), 240-250.https://doi.org/10.1016/j.jrmge.2014.03.006
Nasir, O., and Fall, M. 2008. "Shear behaviour of cemented pastefill-rock interfaces." *Engineering Geology*, 101(3-4), 146-153.10.1016/j.enggeo.2008.04.010
Peron, H., Hueckel, T., and Laloui, L. 2007. "An improved volume measurement for determining soil water retention curves." *Geotechnical Testing Journal*, 30(1), 1-8.https://doi.org/10.1520/GTJ100167
Pineda, J., Alonso, E., and Romero, E. 2014. "Environmental degradation of claystones." *Géotechnique*, 64(1), 64
Seo, H., Prezzi, M., and Salgado, R. 2008 Published. "Settlement analysis of axially loaded piles." *Proc., International Conference on Case Histories in Geotechnical Engineering*.

Shao, J.-F., Jia, Y., Kondo, D., and Chiarelli, A.-S. 2006. "A coupled elastoplastic damage model for semi-brittle materials and extension to unsaturated conditions." *Mechanics of materials*, 38(3), 218-232.https://doi.org/10.1016/j.mechmat.2005.07.002

Sheng, D., Eigenbrod, K. D., and Wriggers, P. 2005. "Finite element analysis of pile installation using large-slip frictional contact." *Computers and geotechnics*, 32(1), 17-26.https://doi.org/10.1016/j.compgeo.2004.10.004

Sisodiya, M., and Zhang, Y. 2020 Published. "A Thermodynamic-Consistent Micro-Crack Damage Model for Brittle Rocks." *Proc., 54th U.S. Rock Mechanics/Geomechanics Symposium*, American Rock Mechanics Association.

Skempton, A. W. 1985. "Residual strength of clays in landslides, folded strata and the laboratory." *Geotechnique*, 35(1), 3-18

Stark, T. D., and Eid, H. T. 1994. "Drained residual strength of cohesive soils." *Journal of Geotechnical Engineering*, 120(5), 856-871

Tian, H. M., Chen, W. Z., Yang, D. S., and Yang, J. P. 2015. "Experimental and Numerical Analysis of the Shear Behaviour of Cemented Concrete-Rock Joints." *Rock Mech Rock Eng*, 48(1), 213-222.10.1007/s00603-014-0560-6

USGS. "Current Water Data for Colorado." <https://waterdata.usgs.gov/co/nwis/gw>.Accessed in (2019)

Van Genuchten, M. T. 1980. "A closed-form equation for predicting the hydraulic conductivity of unsaturated soils 1." *Soil science society of America journal*, 44(5), 892-898.https://doi.org/10.2136/sssaj1980.03615995004400050002x

Wayllace, A., and Lu, N. 2012. "A Transient Water Release and Imbibitions Method for Rapidly Measuring Wetting and Drying Soil Water Retention and Hydraulic Conductivity Functions." *Geotechnical Testing Journal*, 35(1), 103-117.https://doi.org/10.1520/GTJ103596

Wong, R. H. C., Chau, K. T., and Wang, P. 1996. "Microcracking and grain size effect in Yuen Long marbles." *International Journal of Rock Mechanics and Mining Sciences & Geomechanics Abstracts*, 33(5), 479-485.https://doi.org/10.1016/0148-9062(96)00007-1

Zhang, F., Hu, D. W., Xie, S. Y., and Shao, J. F. 2014. "Influences of temperature and water content on mechanical property of argillite." *European Journal of Environmental and Civil Engineering*, 18(2), 173-189.10.1080/19648189.2013.852485

Zhang, F., Jia, Y., Bian, H. B., and Duveau, G. 2013. "Modeling the influence of water content on the mechanical behavior of Callovo–Oxfordian argillite." *Physics and Chemistry of the Earth, Parts A/B/C*, 65, 79-89.https://doi.org/10.1016/j.pce.2013.05.007

FIGURE CAPTIONS

Fig. 1. Vapor equilibrium technique: : (a) Experimental setup; (b) Variation of specimen mass with time in the driest desiccator (RH=11.31%).

Fig. 2. Direct shear box: (a) parts; (b) assembled and connected to the shearing machine.

Fig. 3. Experimental SWRC data fitted with Van Genuchten equation

Fig. 4. Typical load-displacement curves from direct shear testing.

Fig. 5. Pictures of specimens before and after shearing: (a) specimen prepared at low suction; (b) specimen prepared at high suction.

Fig. 6. Mohr-Coulomb envelopes for Site-1: (a) peak strength; (b) residual strength.

Fig. 7. Mohr-Coulomb envelopes for Site-2: (a) peak strength; (b) residual strength.

Fig. 8. Mohr-Coulomb envelopes for Site-3: (a) Peak strength (b) Residual Strength.

Fig. 9. Variation of friction angle with suction: (a) peak friction angle; (b) residual friction angle.

Fig. 10. Variation of peak cohesion with suction. Open symbols denote the additional data from direct shear tests on fully saturated specimens.

Fig. 11. Geometry and boundary conditions of the finite element model.

Fig. 12. Schematics of the simulated steps.

Fig. 13. Saturation contours for 16 hours wetting: (a) Site-1 (b) Site-2 (c) Site-3.

Fig. 14. Workflow of USDFLD subroutine.

Fig. 15. Load-displacement curves for (a) Site-1 (b) Site-2 (c) Site-3.

Fig. 16. Variation of ultimate axial capacity with wetting time for all sites.

Fig. 17. Effect of (a) Saturated hydraulic conductivity (b) In-situ water table depth on variation of ultimate axial load capacity with wetting time.

Fig. 18. Reduction in normalized ultimate axial load capacity with increasing wetting time for different depths of in-situ water table.

Table 1. Index properties of the claystone specimens

	Site		
	1 (Colfax)	2 (Wadsworth)	3 (Wads)
Liquid Limit (%)	67.3-75.3	32.8-44.1	29.7-48.7
Plasticity Index (%)	14.1-39.3	6.7-13.1	1.9-23.6
Water content (%)	28-36	13-18	10-15
Dry unit weight (kN/m^3)	13.6-15.2	17.4-20.2	16.7-18.3
Saturated unit weight (kN/m^3)	19.2-30.6	20.1-27.4	21.6-23.74
Specific gravity of solids	2.70	2.69	2.65

Table 2. Salt solutions used in the Vapor equilibrium method

Salt Solution	Average Relative Humidity (%)	Average Suction (MPa)
Lithium Chloride (*LiCl)*	11.31	294.29
Potassium Carbonate (K_2CO_3)	43.16	113.46
Sodium Chloride (*NaCl*)	75.47	38
Potassium Sulphate (K_2SO_4)	97.59	3.29

Table 3. van Genuchten parameters for the claystone samples in this study

Site	$\alpha\left(kPa\right)^{-1}$	S_r	n
1	0.0005	0.00	1.35
2	0.0008	0.00	1.32
3	0.0015	0.01	1.37

Table 4. Saturated Hydraulic conductivity

Site	Cell pressure (kPa)	Backpressure (kPa)	Initial head difference (m)	Sat. Hydraulic conductivity (m/sec)
1	69	34.5	1.973	2.17×10^{-10}
2	69	34.5	0.222	2.44×10^{-08}
3	69	34.5	0.222	5.73×10^{-08}

Table 5. Peak and residual Mohr-Coulomb parameters

Site	Suction $\psi\left(MPa\right)$	Peak friction angle $\phi_p\left(\deg.\right)$	Peak cohesion $c_p\left(kPa\right)$	Residual friction angle $\phi_r(\deg.)$
1	294.29	56.31	300	40.36
	113.46	54.46	270	36.87
	38.00	50.19	210	30.96
	3.29	41.99	100	26.57
2	294.29	45.00	200	39.35
	113.46	41.99	150	30.96
	38.00	36.87	120	30.11
	3.29	30.96	80	22.29
3	294.29	60.26	440	43.53
	113.46	57.99	380	40.36
	38.00	54.46	300	34.99
	3.29	45.00	190	30.96

Table 6. Parameters for the fitted relation between strength and suction pressure

Site	a_p	a_r	$c_{p1}\left(kPa\right)$	$c_{p2}\left(kPa\right)$
1	0.2696	0.1458	10.28	9.625
2	0.1753	0.1308	28.18	5.055
3	0.3107	0.1668	72.00	11.740

Table 7. Parameters for finite-element simulation

Properties	Claystone			Concrete
	Site-1	Site-2	Site-3	
Saturated unit weight or density (kN/m^3)	25.1	24.0	22.9	23.6
Young's modulus (GPa)	3.35	3.35	3.35	27.00
Poisson's ratio	0.2	0.2	0.2	0.15
Saturated hydraulic conductivity (m/sec)	2.17×10^{-10}	2.44×10^{-8}	5.73×10^{-8}	-

Table 8. Percentage reduction in the ultimate axial load capacity for all three sites

Wetting time (in hours)	Reduction of ultimate axial capacity		
	Site-1 (%)	Site-2 (%)	Site-3 (%)
2	0	13.46	9.33
4	0	18.65	14.77
8	0	26.30	22.54
16	0	31.80	33.16

Table 9. Baseline parameters for the parametric study.

Strength parameters				SWRC parameters			Sat. Hydraulic conductivity(m/sec)
a_p	a_r	$c_{p1}(kPa)$	$c_{p2}(kPa)$	$\alpha(kPa)^{-1}$	S_r	n	
0.3107	0.1668	72.00	11.740	0.5	0.01	1.24	5.73×10^{-08}

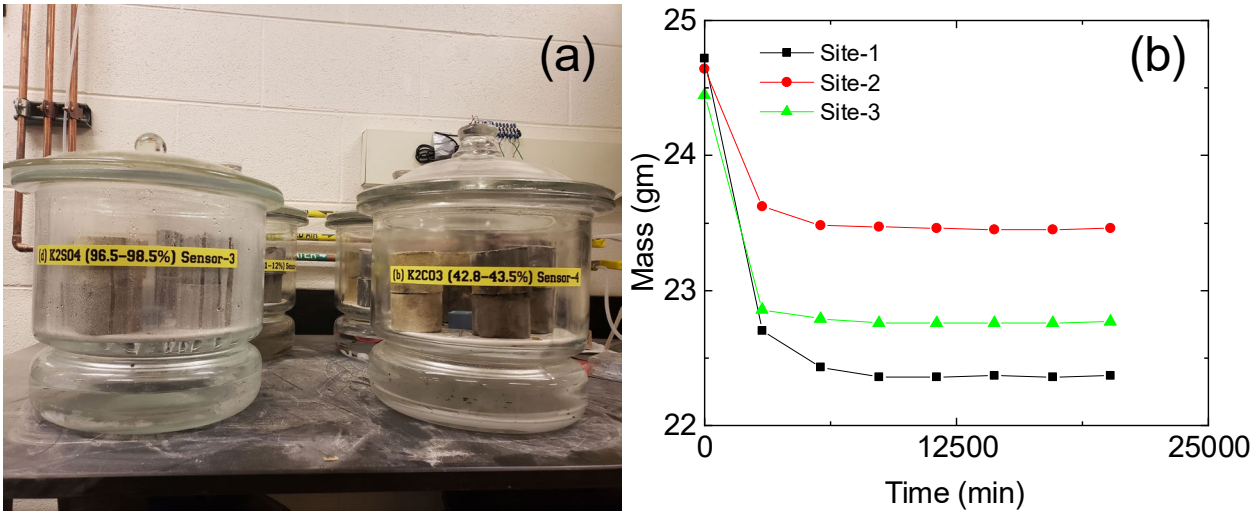

Fig. 1. Vapor equilibrium technique: : (a) Experimental setup; (b) Variation of specimen mass with time in the driest desiccator (RH=11.31%).

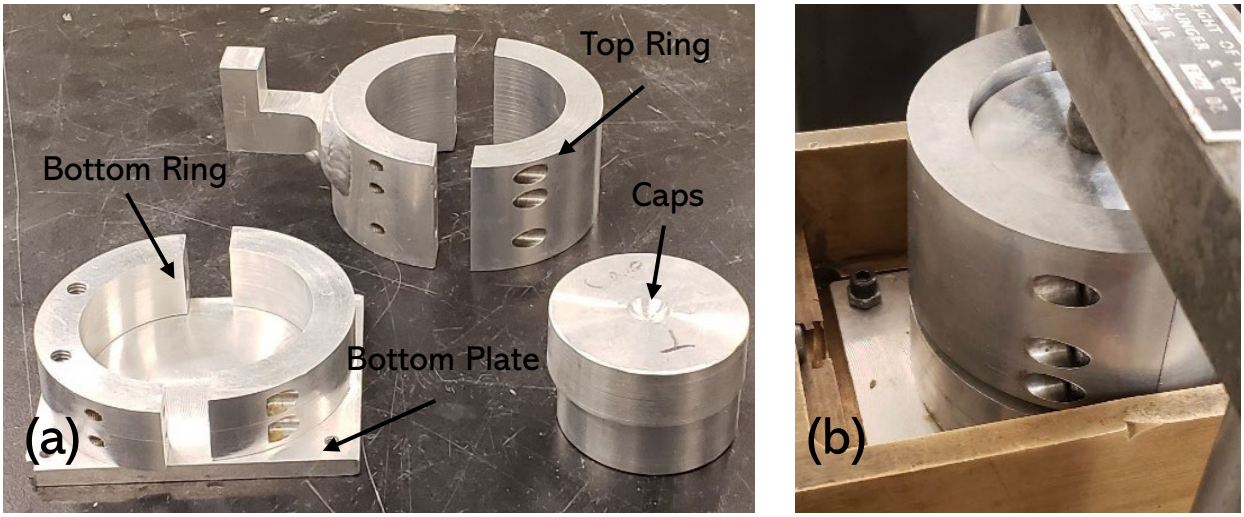

Fig. 2. Direct shear box: (a) parts; (b) assembled and connected to the shearing machine.

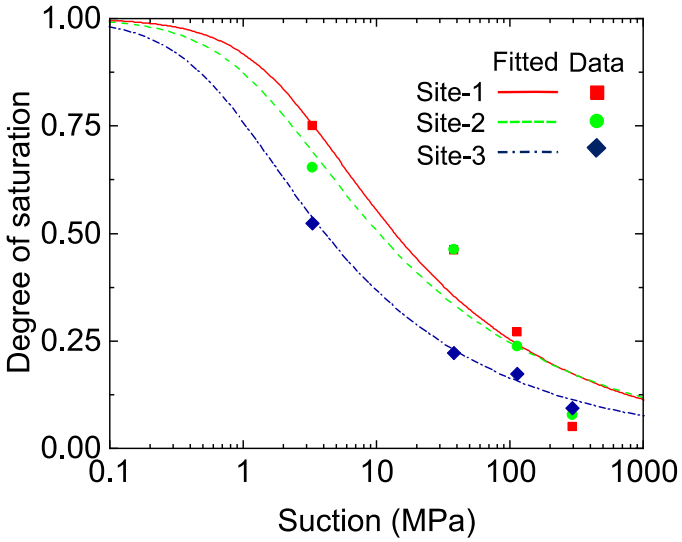

Fig. 3. Experimental SWRC data fitted with Van Genuchten equation

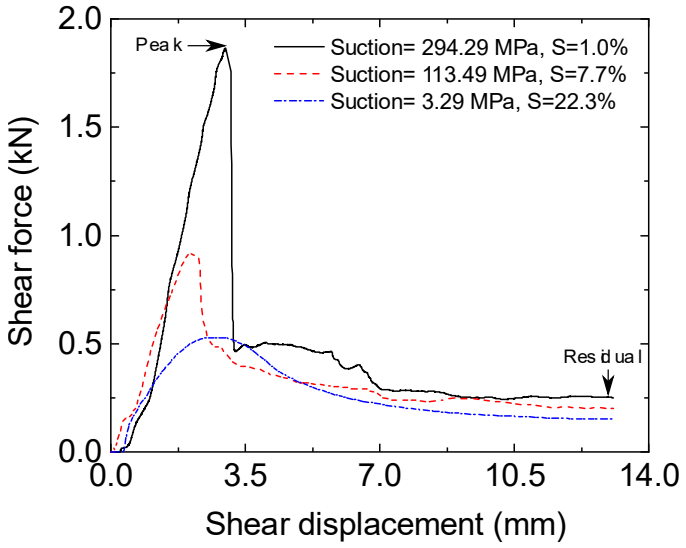

Fig. 4. Typical load-displacement curves from direct shear testing.

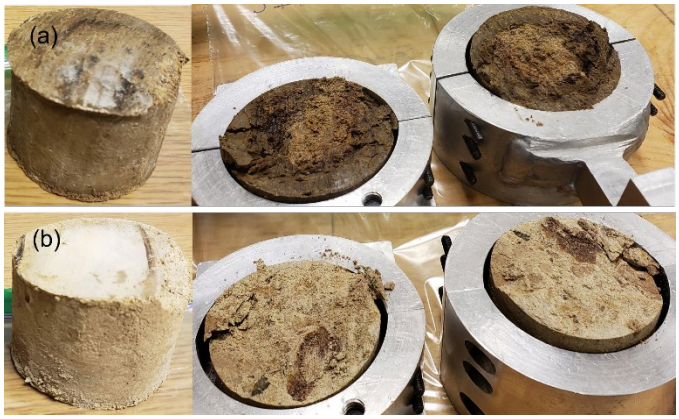

Fig. 5. Pictures of specimens before and after shearing: (a) specimen prepared at low suction; (b) specimen prepared at high suction.

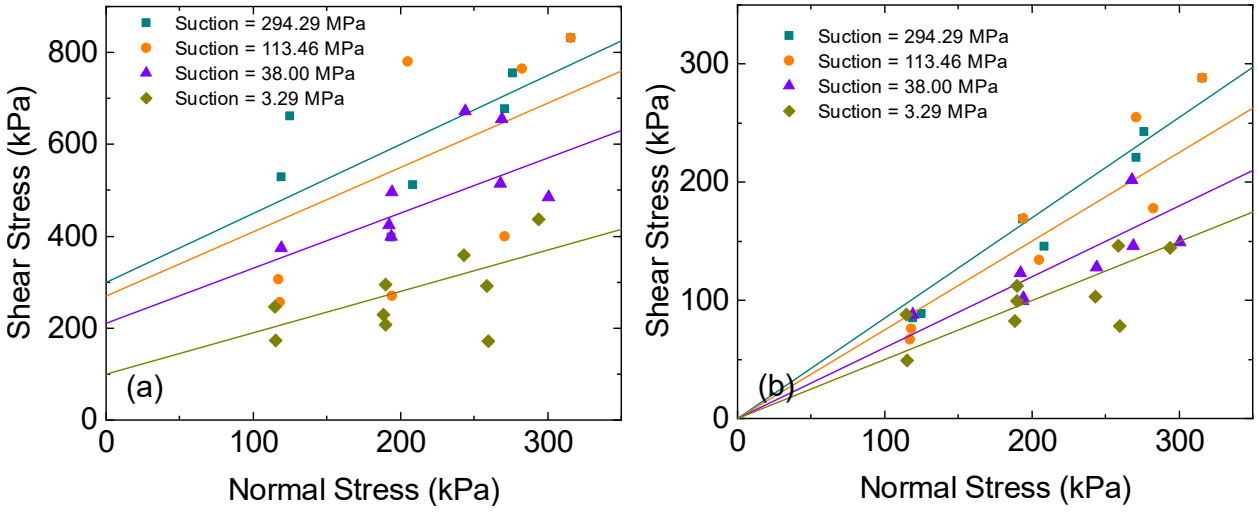

Fig. 6. Mohr-Coulomb envelopes for Site-1: (a) peak strength; (b) residual strength.

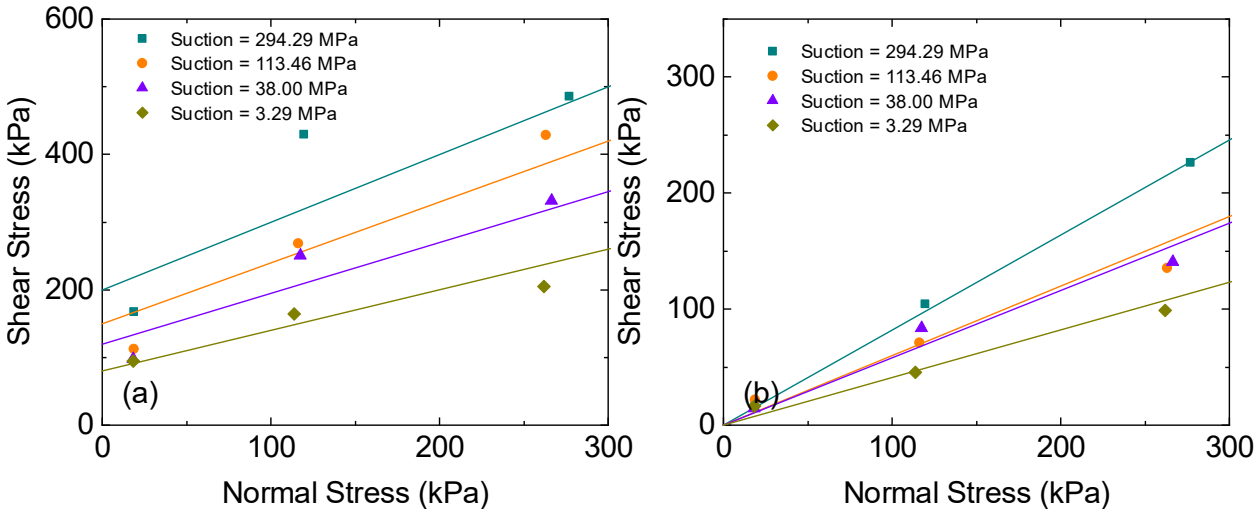

Fig. 7. Mohr-Coulomb envelopes for Site-2: (a) peak strength; (b) residual strength.

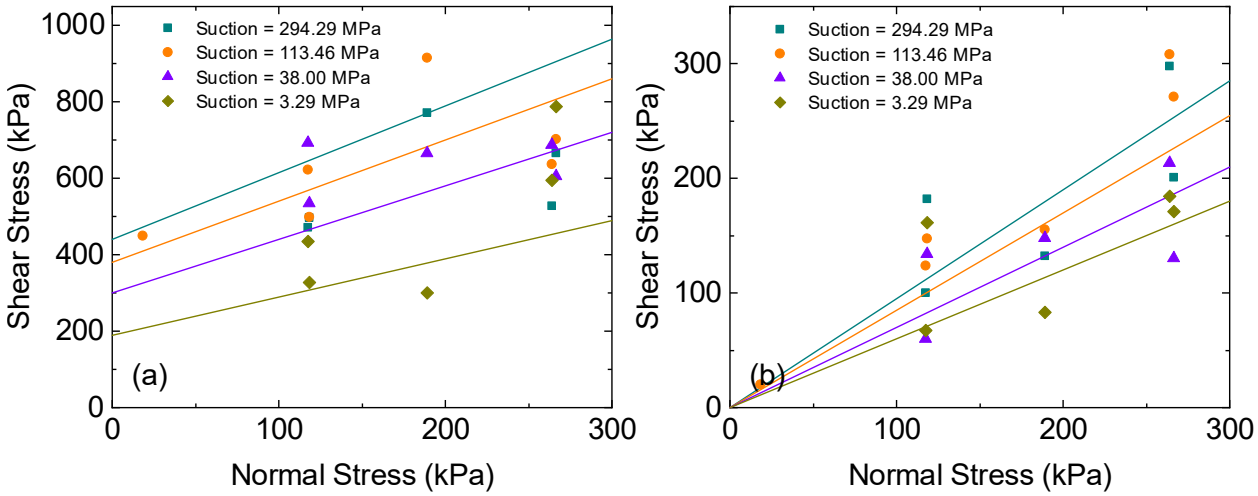

Fig. 8. Mohr-Coulomb envelopes for Site-3: (a) Peak strength (b) Residual Strength.

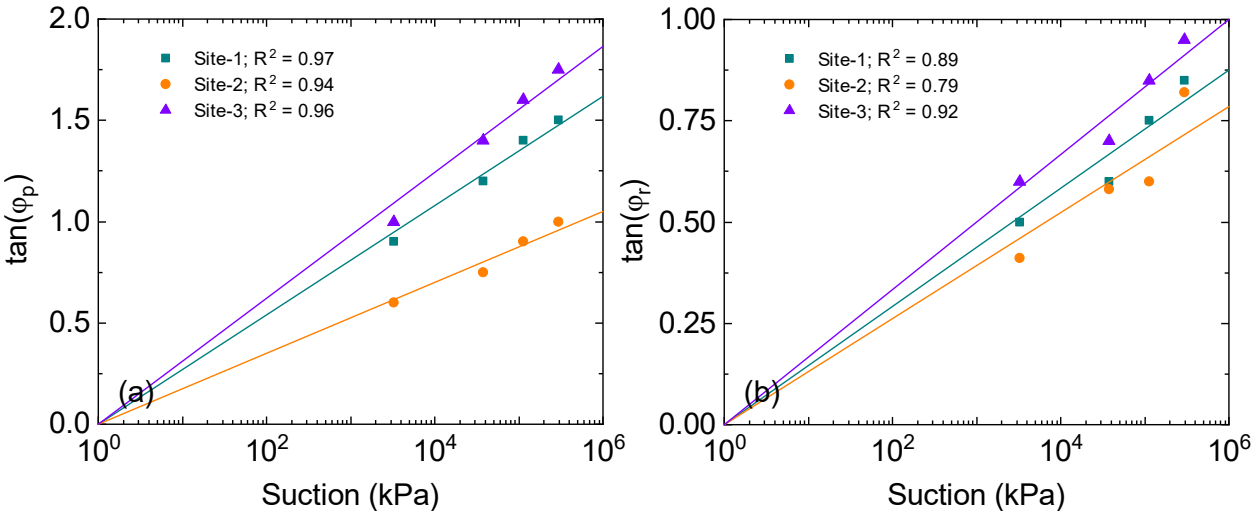

Fig. 9. Variation of friction angle with suction: (a) peak friction angle; (b) residual friction angle.

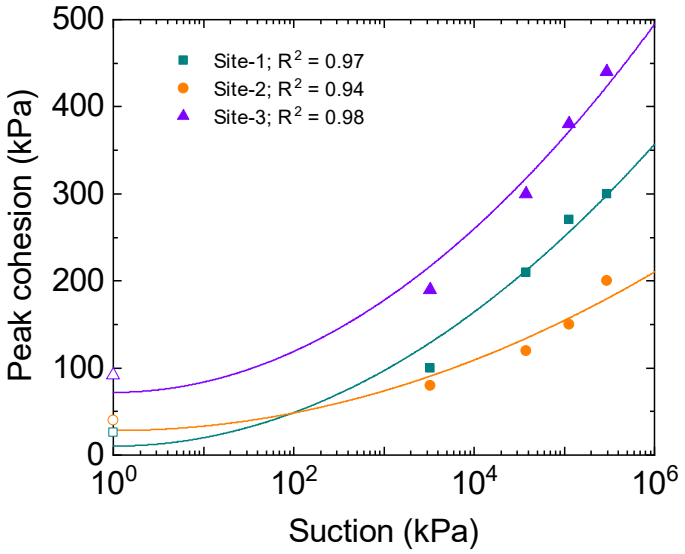

Fig. 10. Variation of peak cohesion with suction. Open symbols denote the additional data from direct shear tests on fully saturated specimens.

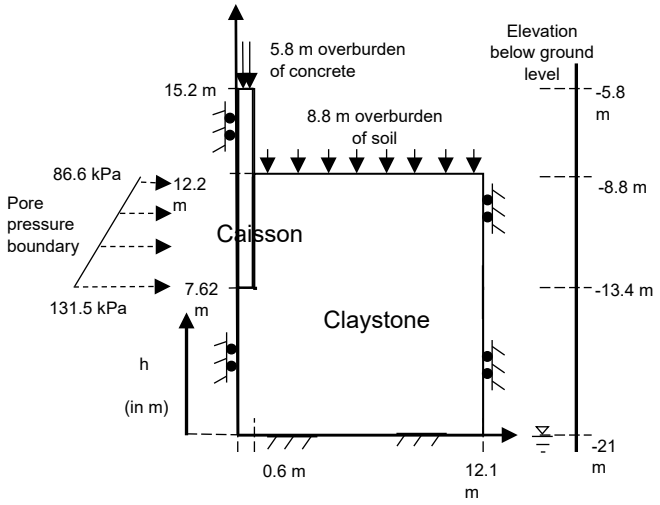

Fig. 11. Geometry and boundary conditions of the finite element model.

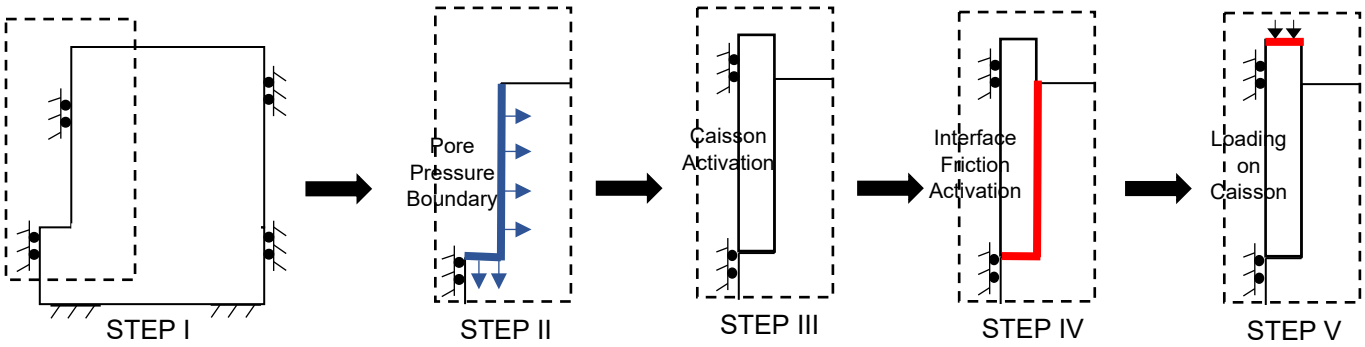

Fig. 12. Schematics of the simulated steps.

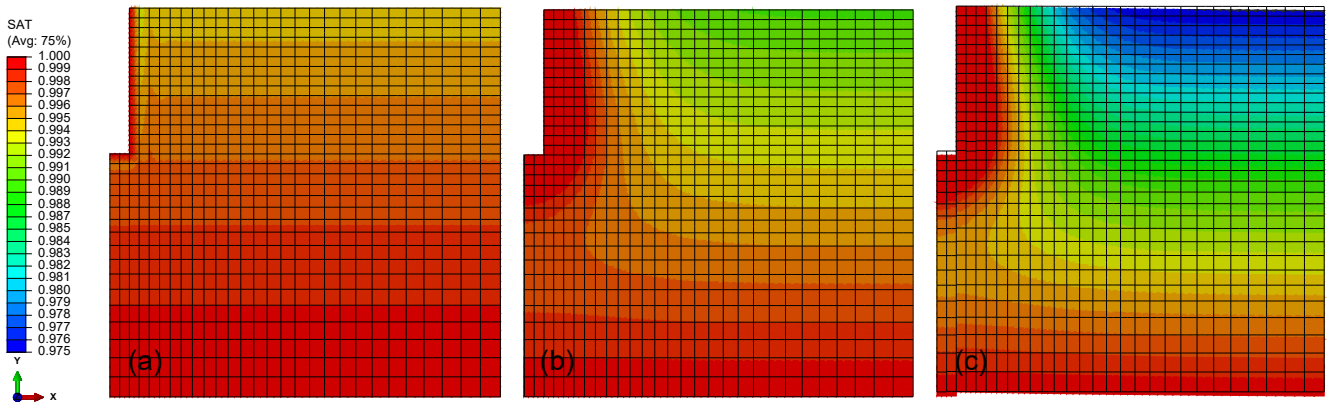

Fig. 13. Saturation contours for 16 hours wetting: (a) Site-1 (b) Site-2 (c) Site-3.

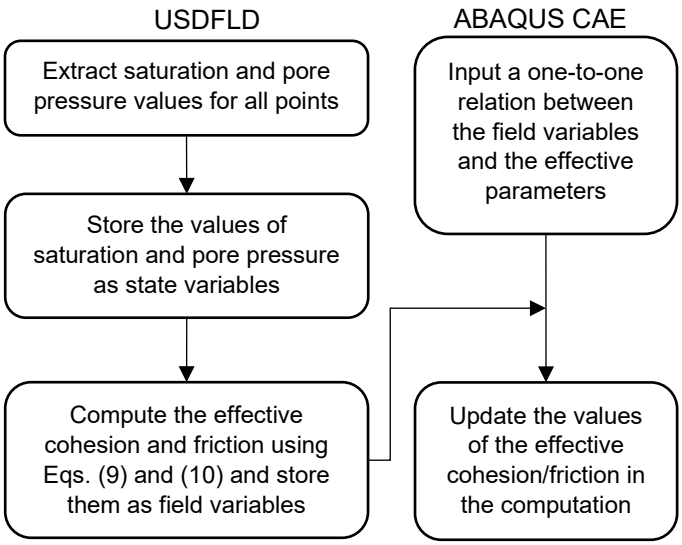

Fig. 14. Workflow of USDFLD subroutine.

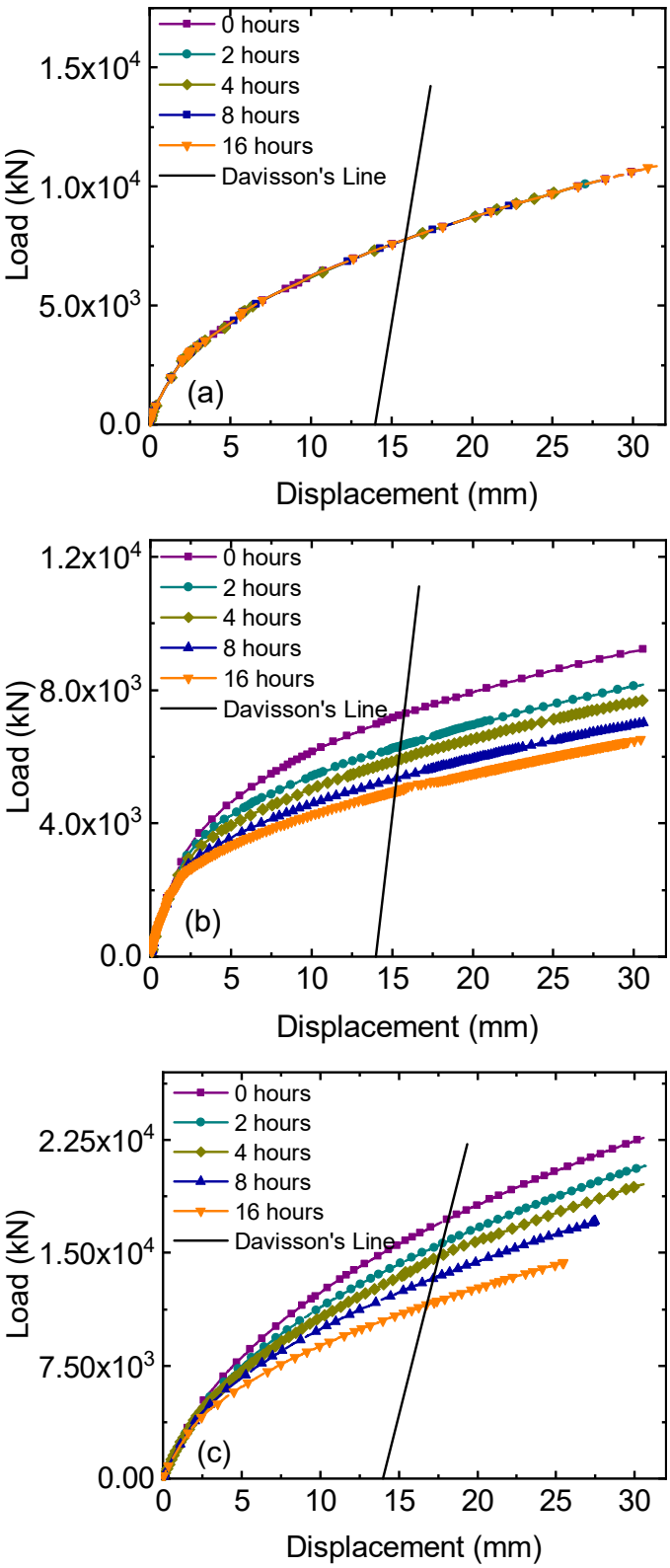

Fig. 15. Load-displacement curves for (a) Site-1 (b) Site-2 (c) Site-3.

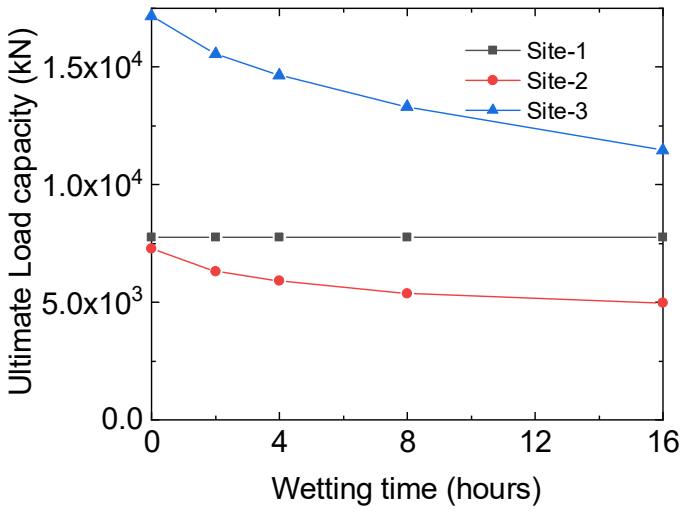

Fig. 16. Variation of ultimate axial capacity with wetting time for all sites.

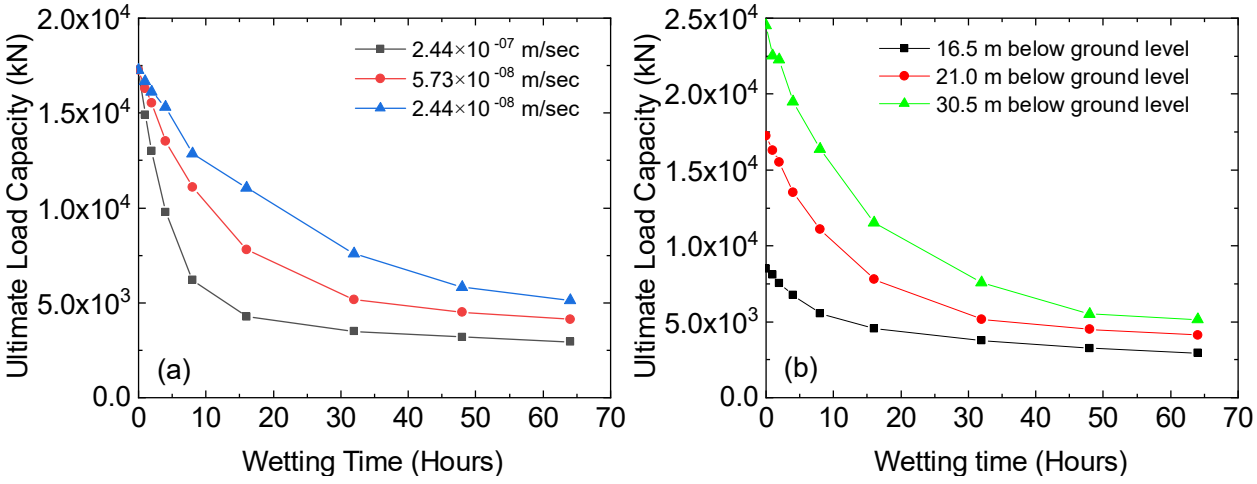

Fig. 17. Effect of (a) Saturated hydraulic conductivity (b) In-situ water table depth on variation of ultimate axial load capacity with wetting time.

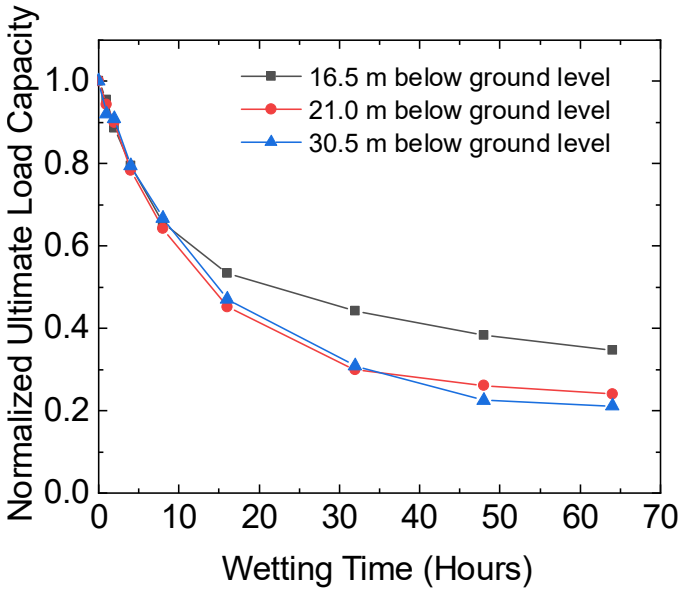

Fig. 18. Reduction in normalized ultimate axial load capacity with increasing wetting time for different depths of in-situ water table.